

A parametric finite element study of concrete cone failure in headed bars under tensile loading

João Paulo de Barros Santos^{a*} , Marcos Honorato de Oliveira^a , Nataniel Wontoon Barbosa Lima^a , Manoel José Mangabeira Pereira Filho^b , Mauricio de Pina Ferreira^b 

^a Departamento de Engenharia Civil e Ambiental, Universidade de Brasília, Brasília, Distrito Federal, Brasil. Emails: joaopaulo_bsantos@hotmail.com, marcoshonorato@unb.br, nwontoon@gmail.com.

^b Núcleo de Desenvolvimento Amazônico em Engenharia, Universidade Federal do Pará, Belém, Pará, Brasil. Emails: manojmangabeira@hotmail.com, mpina@ufpa.br.

* Corresponding author

<https://doi.org/10.1590/1679-78257940>

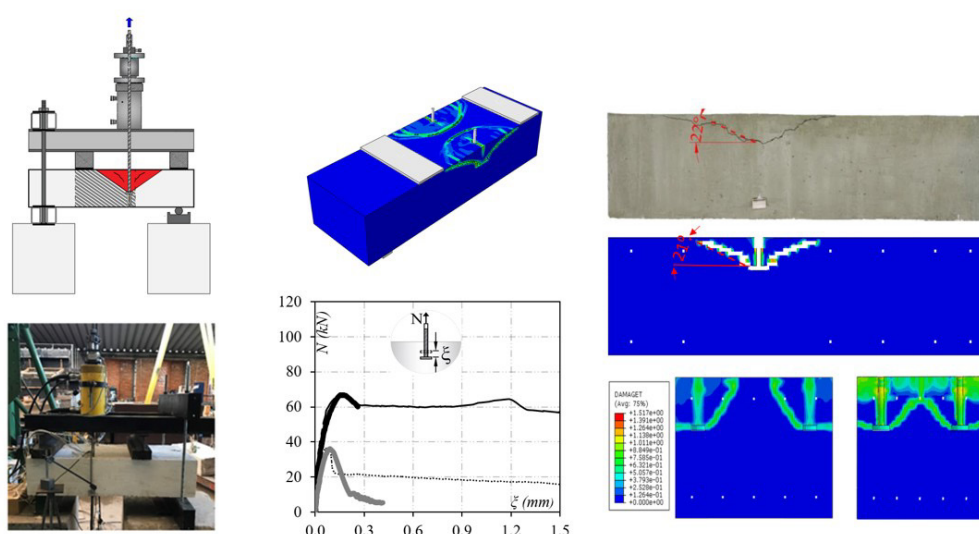
Abstract

This article presents a parametric numerical study of the pullout behavior of headed bars embedded in concrete elements. The finite element model was developed using Abaqus software and validated to simulate the behavior of four pullout tests. The numerical results were validated against the experimental results and showed excellent agreement with the load–slip response and failure modes. Furthermore, a parametric numerical study with 23 simulations was planned to explore the influence of several variables on concrete cone failure, including concrete strength, flexural reinforcement ratio, geometry and head size, shaft diameter, and edge and group effects. The ultimate load results, failure modes, and influence on ultimate load are discussed.

Keywords

Headed bar, Concrete cone failure, Finite element analysis, Parametric study, Abaqus.

Graphical Abstract



Received: November 17, 2023. In revised form: January 17, 2024. Accepted: January 29, 2024. Available online: January 30, 2024.

<https://doi.org/10.1590/1679-78257940>

 Latin American Journal of Solids and Structures. ISSN 1679-7825. Copyright © 2024. This is an Open Access article distributed under the terms of the [Creative Commons Attribution License](https://creativecommons.org/licenses/by/4.0/), which permits unrestricted use, distribution, and reproduction in any medium, provided the original work is properly cited.

1 INTRODUCTION

At the beam-column connections of reinforced concrete structures, the tensile load is most commonly transferred using straight bars or hooks, which, under geometric limitations, combined with reinforcement by a large diameter, may not allow for the adequate development of anchorage in the structure because it does not adapt to the size of the structural element and, consequently, can cause reinforcement congestion (Abed et al. 2021). In turn, reinforcement congestion can lead to poor concrete consolidation in a critical location where the concrete is under a complex state of stress. It can compromise the anchorage strength of the beam-column connection (Marchetto 2015).

As an alternative to hook termination and straight bars, a headed bar is used to minimize the development of embedment lengths and to simplify design detailing (Chourasia and Gupta, 2019). This device is formed by a steel plate fixed to a steel reinforcement by friction welding, a forging process, a threaded connection, or a conical thread (Alrasyid et al. 2017). When subjected to tensile loading, it exhibits the following failure modes: steel failure, pullout failure, side-face blowout, concrete splitting failure, and concrete cone failure (Hayek 2023) (Figure 1). The specific failure mode depends on parameters such as concrete compressive strength, embedment depths, steel strength, edge distance, spacing between headed bars, and other variables, as discussed in detail by Karmokar et al. (2021).

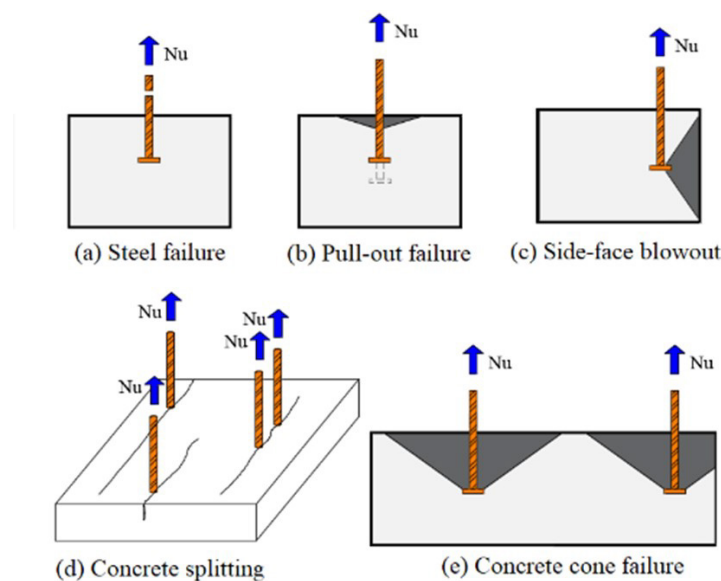


Figure 1. Failure modes of single cast-in anchors under tensile loading.

In recent decades, the successful use of a headed bar as a replacement for the traditional method has been demonstrated in experimental research studies by DeVries (1996), Thompson et al. (2005), Ghimire et al. (2019), Ferreira et al. (2021), and Santana et al. (2022). These studies investigated concrete cone failure under various installation conditions and provided valuable results to validate and improve existing normative calculation models. However, the complex mechanism of transferring tensile loading via the beam-column connection in a concrete structure means that regulatory provisions still require advances to establish adequate calculation criteria. The Concrete Capacity Design (CCD), developed by Fuchs et al. (1995), is the base design method of the standard ACI 318 (ACI Committee 318, 2019) for estimating the tensile response of headed bars. However, the CCD method is a semi-empirical design method with restricted anchor configurations and consequently relies heavily on test data (Bokor et al. 2019). This method was designed to calculate headed connectors; therefore, the bond between the shaft and the concrete is not considered in the tensile strength of the anchor calculations (Chourasia and Gupta 2019). Another crucial factor is that this method establishes that the stress distribution from the device head to the concrete surface presents a linear behavior. However, research by Ožbolt et al. (1999) and Elfgren et al. (1982) concluded that the stress decreases from the head to the surface of the concrete nonlinearly, different from what the CCD method establishes. Therefore, simplifying the method may lead to conservative results in accurately determining the tensile force of headed bars (Lai et al. (2023). In addition, most studies on the subject are experimental research focused on headed bars in concrete without edge and group effects. Therefore, there needs to be more research on numerical simulations that explore concrete cone failure and the tensile strength of the anchors, with simultaneous edge and group effects.

This study conducted a comprehensive numerical investigation of the behavior of headed bars embedded in concrete elements under tensile loads with edge and group effects, including aspects such as load–slip curves and failure modes. The experimental tests from Lima's (2019) research were essential to calibrate and validate the 3D nonlinear finite element model developed in the Abaqus software. Material constitutive models, the interfacial bond-slip relationships between the headed bar and the concrete, and an explicit dynamic analysis were adequately established to represent the pullout behavior of a headed bar. The numerical results showed that the proposed numerical model adequately describes the behavior of the headed bar under tensile load under edge and group effects. Additionally, a parametric numerical study with twenty-three models was developed to investigate the influence of several parameters on concrete cone failure and the tensile strength of the anchors, including concrete compressive strength, flexural reinforcement ratio, shape and head size, shaft diameter, edge and group effects.

2 METHODOLOGY USED FOR THE NUMERICAL MODELLING

2.1 General Objective

This study aims to develop a nonlinear 3D finite element model with Abaqus software to simulate the pullout behavior of headed bars embedded in concrete elements under edge and group effects and to evaluate the influence of various parameters on the tensile strength of these headed bars. For this purpose, an explicit dynamic analysis was adopted in this study, as this procedure is suitable for describing static and quasi-static phenomena involving complex problems of contact, damage, and failure of materials, such as interfacial slippage between steel and concrete, cracking, and concrete crushing (Lima et al. 2020).

In modeling the nonlinear behavior of concrete, the Concrete Plasticity Damage (CPD) model available in the Abaqus software was adopted. This model simulates plasticity and damage in concrete based on the principles of the finite element method. The accuracy of the CDP crucially depends on the proper calibration of the plasticity parameters, the adequate description of the uniaxial behavior of concrete under tension and compression, and the evolution of concrete damage. This calibration is essential to ensure that the responses of the numerical model align with the pullout of head studs from experimental tests.

In parallel, the behavior of steel was modeled using the elastic-perfectly plastic model. This model simplifies the material response by assuming a direct transition from elastic to plastic behavior without hardening, which is suitable for this application. Previous studies by Santana et al. (2022) and Lai et al. (2023) successfully numerically simulated the pullout of headed bars embedded in concrete elements using an explicit dynamic analysis.

2.2 Experimental Tests

The reference experimental program was taken from research by Lima (2019) developed at the Structures Laboratory of the University of Brasília (UnB). This research included the development of four test specimens to evaluate the pullout of a headed bar under edge and group effects. These trials were divided into two groups: E and G. Group E assessed the influence of the edge effect, while Group G evaluated the simultaneous edge and group effect.

In group E, the specimens were designated as E-60 and E-120, representing specimens with edge effects and effective embedment depths (h_{ef}) of 60 mm and 120 mm, respectively. In both specimens, the edge distance, c_{a1} , was equal to 52 mm. The spacing, s , between the headed bars was defined as being $s = 181$ mm and 361 mm for the E-60 and E-120 specimens, respectively. The headed bar was defined with a head diameter three times larger than the diameter of the shaft, which is by ACI 318 (ACI Committee 318, 2019) and ASTM A970 (2018) standards. Thus, the analysis ratios were defined as $0.4 < c_{a1}/h_{ef} < 0.9$ to represent the edge effect and $s/h_{ef} = 3.0$ as established by the ACI 318 (2019) and EN 1992-4 (2018) standards to avoid the overlap of concrete cone failure and to represent the absence of group effect.

On the other hand, group G was designed to evaluate the simultaneous influence of edge and group effects. The specimens were designated as G-60 and G-120, representing specimens with 60 mm and 120 mm effective embedment depths, respectively. The specimens maintained the same c_{a1}/h_{ef} ratios defined in group E and the geometry of the head bar. However, there was an intentional reduction in the spacing of the bars in a group (s) and in the width (bw) of the specimens to achieve a $2.0 < s/h_{ef} < 3.0$ ratio necessary to ensure the overlap of the projections of the failure surfaces of the concrete cones.

The concrete specimens had fixed dimensions of $h = 250$ mm and $L = 1100$ mm, and b_w varied according to the analyzed model. The flexural reinforcements had a ratio, ρ_f , between 1.27% and 1.75%, and the stirrups had a rectangular shape that followed the shape of the concrete specimen according to its width b_w . The flexural reinforcement and stirrups were manufactured from CA-50 and CA-60 steel, respectively. The shaft was manufactured from CA-50 steel, and the head was manufactured from ASTM A970M (2018) steel. Table 1 summarizes the details and mechanical properties of the materials, and Figure 2 presents the test system and details of the concrete specimen.

Table 1. Specimen testing details.

Specimen Name	Headed Bar						Flexural reinforcement					Analysis ratio	
	b_w (mm)	h_{ef} (mm)	c_{a1} (mm)	s (mm)	f_y (MPa)	E_s (MPa)	n°	ϕ_f	f_y (MPa)	E_s (MPa)	ρ_f (%)	c_{a1}/h_{ef}	s/h_{ef}
E-60	285	60	52	181	557	181	4	12.5	557	181	1.38	0.9	3.0
E-120	465	120		361			6				1.27	0.4	3.0
G-60	225	60		121			4				1.75	0.9	2.0
G-120	350	120		246			6				1.68	0.4	2.1

Note: $f_{cm} = 47.6$ MPa, $f_{tm} = 3.38$ MPa; $E_c = 39.0$ GPa; $L = 1100$ mm; $h = 250$ mm.

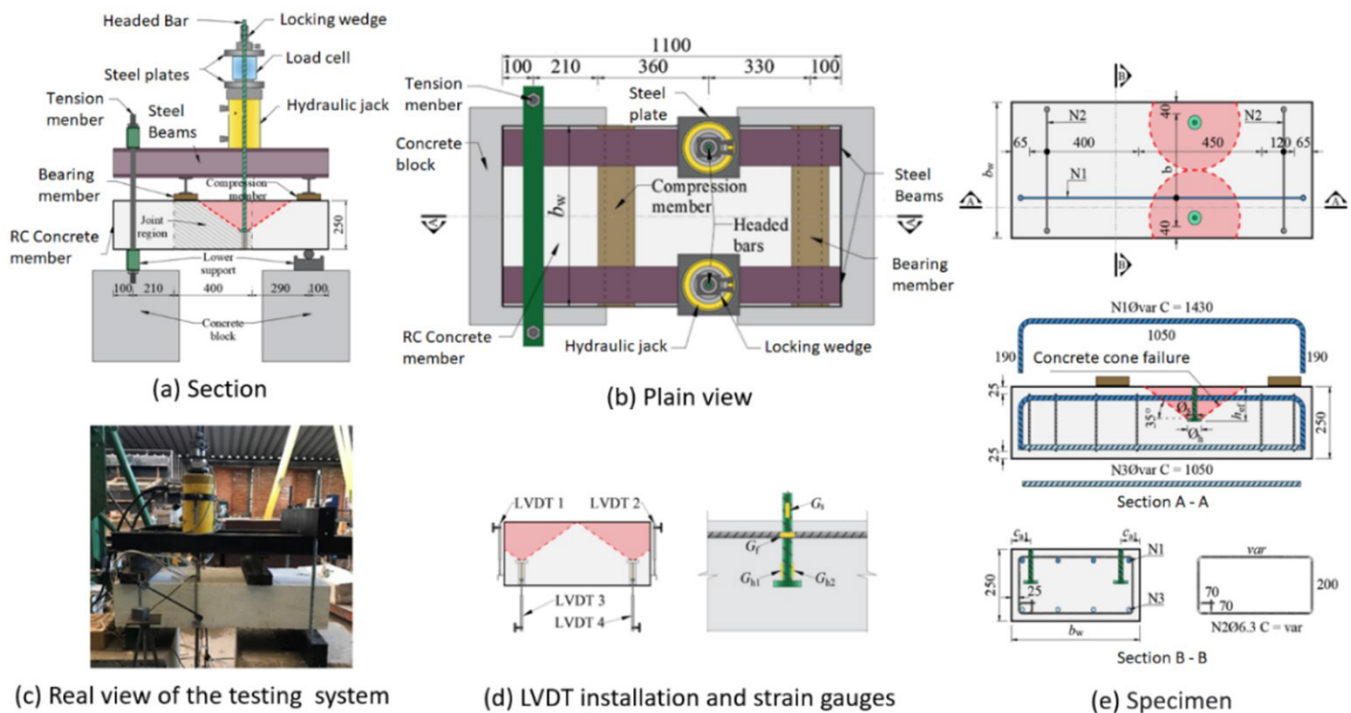


Figure 2. Test setup and construction details of the experimental models.

The effective embedment depths increased the ultimate load $N_{u,EXP}$ in all specimens regardless of the working group. In specimens E-60 and E-120 from group E, there was an increase of 84% when h_{ef} varied from 60 mm to 120 mm. Similarly, in specimens G-60 and G-120 of group G with edge and group effects, there was an increase of 131.5% when h_{ef} varied from 60 mm to 120 mm. The group effect G tended to reduce the ultimate load value by 14% on average for specimens with $h_{ef} = 60$ mm. Quantifying the edge effect was impossible because all specimens were the same distance from the edge. However, being close to the edge produces the same effect as the presence of cracks in the concrete since the cone can't develop into a complete shape, reducing the ultimate load (Eligehausen et al. 2006). Concrete cone failure occurred in all experimental tests. The crack started at the head of the device and extended to the surface of the concrete element with an inclination varying between 22° and 32°.

2.3 Finite element, geometry, and mesh size

Abaqus software was used to numerically simulate the pullout behavior of the headed bar under tensile load and embedded in concrete. Then, a nonlinear finite element model was developed. The C3D8R solid hexagonal element with reduced integration with the hourglass control and the eight-node linear brick (Abaqus 2014) was used to model concrete in a region not influenced by concrete cone failure with a mesh size of 25 mm, and with a headed bar with mesh sizes of 5 mm and 10 mm inside and outside the concrete, respectively. The fully integrated solid hexagonal C3D8 linear element (Abaqus 2014) was used to model concrete in the region influenced by concrete cone failure with a mesh size equal to 8 mm, as it is a region with a higher concentration of stresses and deformations. Moreover, the two-node linear 3D truss element was used to model reinforcements embedded in concrete.

2.4 Support conditions, interactions, and load application

The same support conditions as the experimental model were maintained for the numerical simulation. Rotation and displacement constraints were applied to the concrete prism supports, and only a displacement in the direction of the tensile force on the y-axis of the headed bar was allowed. The experimental model was symmetric on the x-axis. Therefore, only half of the numerical model was developed. Then, all model nodes located on this surface (y-z plane) were prevented from translating in the x direction and rotating in the y and z directions, i.e., $U_x = U_{Ry} = U_{Rz} = 0$.

Contact between the concrete surface and the surface of the headed bar and that between the concrete and steel reinforcement were considered perfect bonds as a simplified approximation of the behavior of the materials.

An explicit dynamic analysis was applied to obtain a quasi-static solution (Earij et al. 2017, Shafei and Tariverdilo 2021, and Genikomsou and Polak 2015). Then, a controlled displacement method was applied to describe the application of loading with an amplitude ranging from 0 mm/s to 10 mm/s (Qureshi et al. 2011) so that the kinetic energy (ALLKE) of the deformed structure is not used to extrapolate a small fraction, typically 5%, of its internal energy (ALLIE) during most of the simulation (Abaqus 2014). Figure 3 shows the geometry, types of finite elements, and boundary conditions of the 3D model.

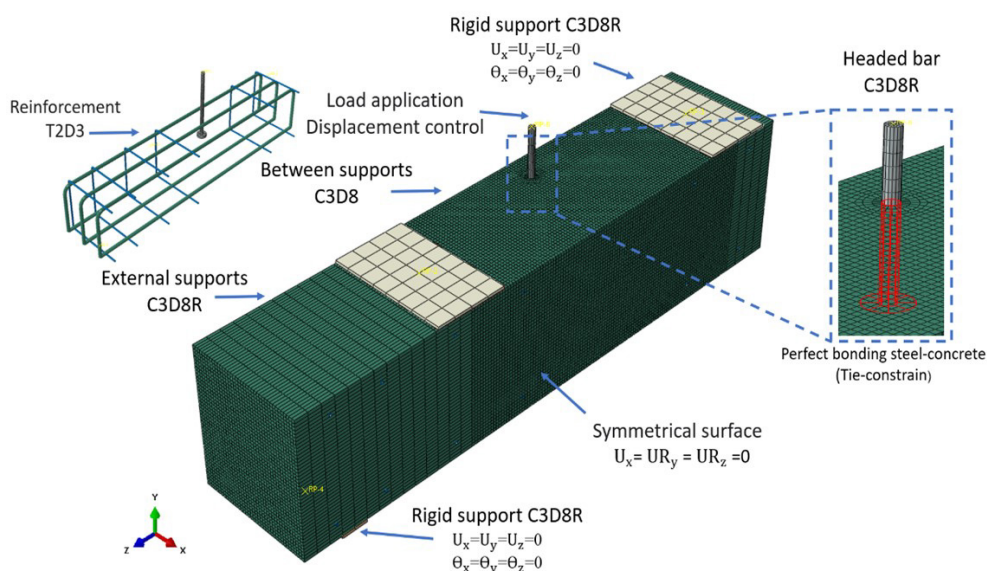


Figure 3. Three-dimensional model.

2.5 Constitutive model of steel

The model adopted to represent the behavior of steel was the perfectly plastic elastic model, alongside the Von Mises yield criterion and yield surface with anisotropic hardening (Lima et al. 2020). The characteristics and properties of the steels from the experimental research are presented in Table 1. Poisson's ratio for the steel was assumed to be equal to 0.3.

2.6 Concrete damage plasticity (CDP)

Concrete Damage Plasticity (CDP) is a model already implemented in Abaqus software and frequently applied to model the nonlinear physical behavior of concrete structures (Ribeiro et al. 2020). According to Lai et al. (2023), it is a modification of the Drucker–Prager resistance hypothesis and was developed by Lubliner et al. (1989) and modified by Lee and Fenves (1998) to consider the evolution of the tensile and compressive strengths of concrete. Microcracks and cracks are represented macroscopically with a smoothing stress-strain response. When concrete is unloaded from any point on the strain attenuation branch of the stress-strain curves, the unloading response is weakened, the elastic stiffness of the material is degraded, and plastic deformation is observed (Ribeiro et al. 2020).

The uniaxial compression behavior of concrete was defined using the stress-strain curve proposed by Alfarah et al. (2017). This curve is composed of three sections: the first section presents linear behavior up to stress equal to 40% of the rupture stress f_{cm} defined by the secant modulus of elasticity E_0 and Poisson's ratio, followed by a parabolic section of hardening up to the breaking strength f_{cm} . Finally, the descending section varies depending on the crushing energy G_{ch} . The uniaxial tensile behavior of concrete has a linear stretch up to f_{tm} , defined as a function of E_0 . The softening behavior of cracked concrete is defined using the stress-strain curve proposed by Hordijk (1992). The concrete Poisson's ratio and specific weight were assumed to be 0.20 and 2.400 kg/m³, respectively. The Concrete Plasticity Damage model equation combines the plastic flow law with the damage evolution law. In a simplified manner, it can be expressed as Equation 1.

$$\sigma = (1 - D) E_0 : (\varepsilon - \varepsilon^{pl}) \quad (1)$$

Where σ is the stress in the concrete, D is the degradation variable, E_0 is the elastic stiffness tensor, ε is the tensor of total strains, and ε^{pl} is the tensor of plastic strains.

For uniaxial compression and tension, the stress-strain relation under uniaxial loading in the damage-plasticity behavior can be written as Equations 2 and 3, respectively.

$$\sigma_c = (1 - d_c) E_0 : (\varepsilon - \varepsilon_c^{pl}) \quad (2)$$

$$\sigma_t = (1 - d_t) E_0 : (\varepsilon - \varepsilon_t^{pl}) \quad (3)$$

Where d_t and d_c are the scalar damage variables, t , and c represent tension and compression, which tend to increase the plastic equivalent stresses; therefore, uniaxial damage variables can take values between 0 for undamaged materials and 1 for entirely damaged materials (Alfarah et al., 2017).

According to Lubliner et al. (1989), when defining a plastic damage model, it is necessary to specify the flow criteria, plastic flow rule, and the evolution of the damage parameters. One of the most common flow criteria is the Drucker-Prager criterion, an extension of the von Mises criterion for cohesive and frictional materials such as concrete. The CDP flow criteria are based on the F function proposed by Lubliner et al. (1989) and improved by Lee and Fenves (1998) to take into account the different evolutions of tensile and compressive strength, according to Equations 4,5 and 6:

$$F = \frac{1}{1 - \alpha} (q - 3\alpha p + \beta \langle \sigma_{\max} \rangle - \gamma - \langle \sigma_{\max} \rangle) - \bar{\sigma}_c = 0 \quad (4)$$

$$\alpha = \frac{(f_{b0} / f_{c0}) - 1}{2(f_{b0} / f_{c0}) - 1}, \quad \beta = \frac{\bar{\sigma}_c}{\bar{\sigma}_t} (1 - \alpha) - (1 + \alpha), \quad \gamma = \frac{3(1 - K_c)}{2K_c - 1} \quad (5)$$

$$K_c = \frac{\rho_{t0}}{\rho_{c0}} = \frac{3 - \text{sen}\phi}{3 + \text{sen}\phi} \quad (6)$$

Where $\langle \cdot \rangle$ are the Macaulay brackets, when the value inside the bracket is negative, its value is zero. When positive, it assumes the parameter's value inside the bracket, p is the hydrostatic pressure, q is the effective Von Mises stress, and d is a scalar damage variable. The proposals $\bar{\sigma}_c$, and $\bar{\sigma}_t$ are the effective evolution and tensile cohesion stresses, respectively.

The K_c parameter is obtained from the Mohr-Coulomb flow surface in polar coordinates, with a value equal to 0.7 when assuming an angle ϕ of 32° , as Alfarah et al. (2017) predicted. Physically, it represents the relationship between the distances from the hydrostatic axis to the meridional plane of traction (ρ_{t0}) and the distance from the hydrostatic axis to the meridional plane of traction (ρ_{c0}).

The plasticity model is predicated on the concept of a non-associated potential plastic flow, where the flow potential, denoted as G , is characterized by the Drucker-Prager hyperbolic function, given by Equation 4.

$$G = \sqrt{\epsilon \sigma_{t0} \tan \psi + q^2} - p \tan \psi \tag{4}$$

Where σ_{t0} represents the stress under uniaxial tension at the point of failure, ϵ indicates the eccentricity associated with the surface of the plastic potential. ψ denotes the angle of dilatancy, which is observed in the p - q plane, commonly referred to as the diverter, under conditions of elevated confining pressure (Alfarah et al. 2017).

The plasticity parameters in the CDP model were defined based on research by Santana et al. (2022), who numerically simulated the pullout of headed bars embedded in concrete as follows: dilatancy angle $\psi = 13^\circ$; eccentricity of the flow potential $\epsilon = 0.1$; $f_{b0}/f_{c0} = 1.16$; and $K_c = 0.7$, obtained from the Mohr-Coulomb flow surface in polar coordinates.

3 VALIDATION OF THE USED METHODOLOGY

3.1 Comparison of experimental vs. numerical load–slip results

Table 2 presents the ultimate load and slip values at failure from the group E and G numerical and experimental models. All numerical and experimental models showed concrete cone failure (CCF). The relationship between the experimental and numerical ultimate loads presented an average equal to $N_{u, EXP}/N_{u, FEA} = 1.02$, and a standard deviation of 0.03. In contrast, the relationship between the experimental and numerical slips in the ultimate load was equal to $\xi_{EXP}/\xi_{FEA} = 0.98$ and a standard deviation of 0.15. These results confirm the excellent agreement between the numerical and experimental models.

Additionally, Figure 4 compares the load–slip curves of groups E and G's experimental and numerical models; the dashed lines represent the experimental behavior, and the solid line represents the numerical behavior. Both groups have excellent agreement between the numerical and experimental curves regarding initial stiffness, ultimate load, and slip. Therefore, the model is suitable for predicting the pullout of headed bars embedded in concrete. A similar phenomenon was observed in the research by Santana et al. (2022) and Lai et al. (2023).

Table 2. Comparison of the numerical vs. experimental ultimate loads.

Model	Experimental Results		Numerical Results			$N_{u,EXP}/N_{u,FEA}$	ξ_{EXP}/ξ_{FEA}
	$N_{u,EXP}$ (kN)	ξ_{EXP} (mm)	$N_{u,FEA}$ (kN)	ξ_{FEA} (mm)	Failure mode		
E-60	36.3	0.07	36.05	0.09	CCF	1.01	0.78
E-120	66.7	0.17	66.91	0.16	CCF	1.00	1.06
G-60	30.8	0.14	30.79	0.12	CCF	1.00	1.17
G-120	71.3	0.11	66.35	0.12	CCF	1.07	0.92
Average						1.02	0.98
Standard deviation						0.03	0.15

Note: CCF: concrete cone failure; ξ : slip.

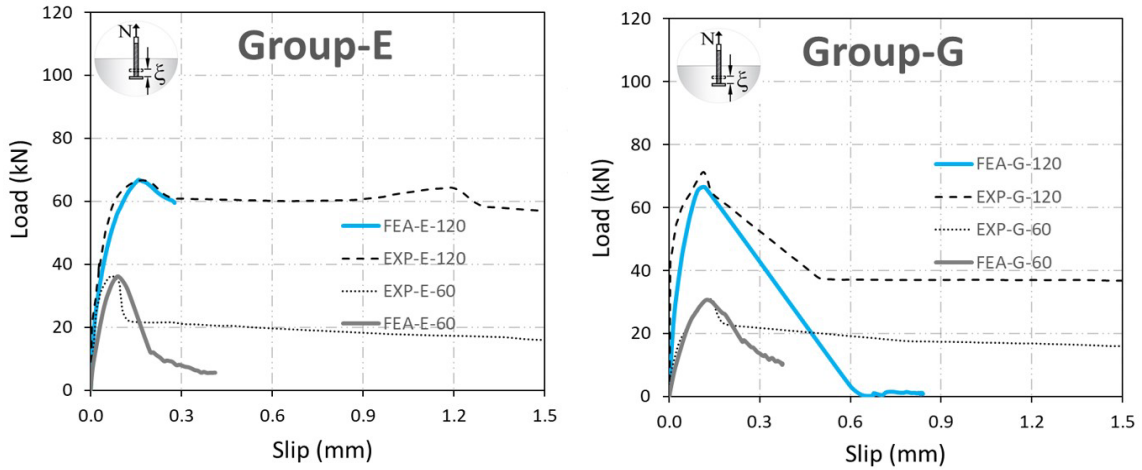


Figure 4. Comparison between numerical and experimental load–slip curves for groups E and G.

3.2 Validation of the quasi-static solution

Validation of the quasi-static solution is necessary to verify the possibility of undesirable inertial effects due to the rapid appearance of cracks in the concrete because of the pullout of the headed bar. This validation is carried out based on the energy balance of the system. As shown in Figure 5 from the kinetic and internal energy history during the headed bar pullout process for all models, the kinetic energy remained low, at less than 5% of the internal energy, as established in Abaqus (2014). Therefore, inertial effects can be neglected. This result agrees with that found in a previous study by Ke et al. (2022).

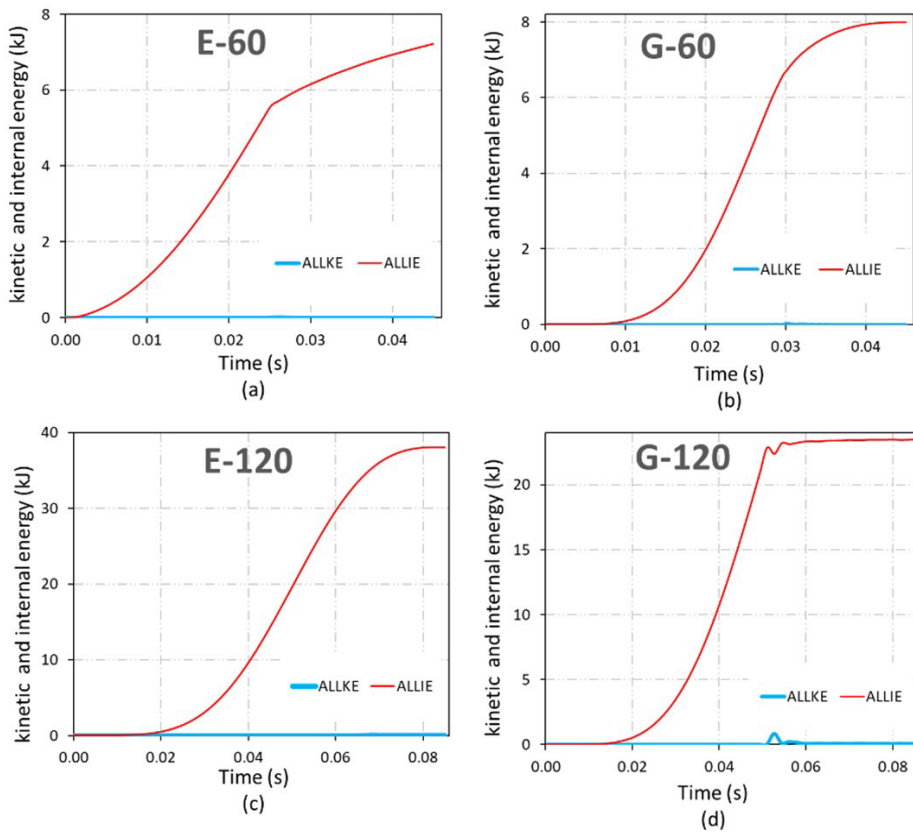


Figure 5. Energy balancing of computational models.

3.3 Cracking Pattern Validation

The cracking patterns of the headed bar from the experimental and numerical models are shown in Figure 6. The variation in the angle of the surface of the concrete cone failure varied between 23° and 29° in the experimental model of group E and from 23° to 32° in group G. In the numerical model, the angle varied between 21° and 33° in group E and from 16° to 28° in group G, showing that the most significant difference found between the angles was 4° in group E and 7° in group G. Therefore, the numerical model adequately captured the concrete cracking behavior from the experimental tests. Additionally, it is possible to verify that the cracking process occurs close to the head of the device, and the cracks propagate towards the upper surface of the concrete and on the lateral surface of the concrete element due to the headed bar being close to the edge. Furthermore, it ultimately divides the concrete into a cone shape.

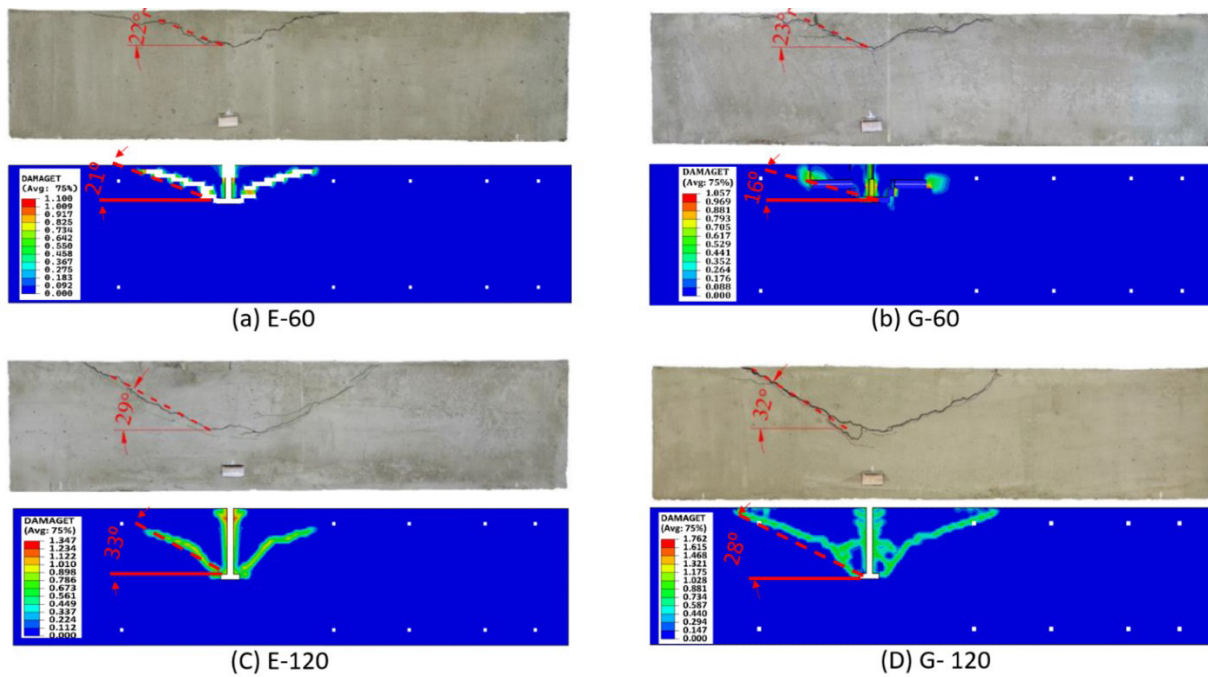


Figure 6. Cracking patterns.

3.4 Validation of the model according to the ACI 318 (2019) standard

The ultimate load results from the numerical models were evaluated against the normative prescriptions of ACI 318 (2019). Figure 7 shows the graph of the ultimate load calculated with ACI 318 (2019) as a function of the ultimate load extracted from the numerical models. It can be concluded that the numerical values of the ultimate load favor safety despite the ACI 318 (2019) standard providing a very conservative estimate of the pullout force of the headed bar.

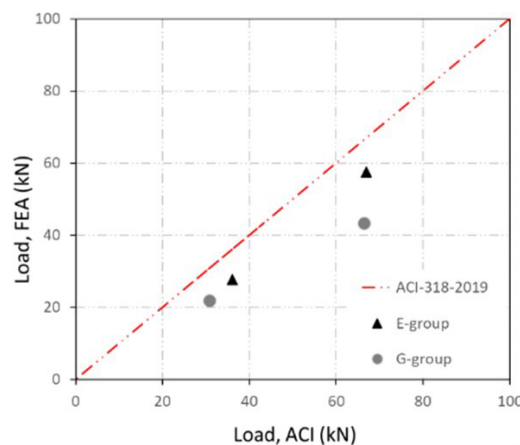


Figure 7. Comparison of ultimate load FEA with ACI 318 (2019).

4 PARAMETRIC INVESTIGATION

After validating the finite element model, a parametric numerical investigation was developed to evaluate the influence of different parameters on the load-slip response and the concrete cone resistance of the headed bars to check the design code limits and recommendations. From the four initial models validated in the previous section, nineteen models were developed, carrying out a total of twenty-three numerical models to investigate the effect of seven parameters that influence the tensile strength of head bars embedded in concrete elements. The following parameters were set to investigate: concrete compressive strength f_{cm} , flexural reinforcement ratio ρ_f , head geometry, shaft diameter $d_{s,L}$, head diameter d_h/h_{ef} , edge effect c_{a1}/h_{ef} , and group effect s/h_{ef} . Table 3 shows the studied parameters. In the analyses presented in this topic, the effect of each parameter on the pullout response and resistance of the headed bars was investigated individually, keeping the values of the other parameters constant.

Table 3. Parametric study variables.

ID	Parameter	Levels		
1	Compressive strength of concrete (f_{cm})	17.7 MPa	32.7 MPa	47.6 MPa
2	Flexural reinforcement ratio (ρ_f);	0.88%	1.38%	2.26%
		1.12%	1.74%	2.86%
3	Head geometry	Circular	Rectangular	Square
4	Shaft diameter ($d_{s,L}$)	10.0 mm	12.5 mm	16.0 mm
5	Head diameter (d_h/h_{ef})	$d_h = 0.31 h_{ef}$	-	$d_h = 0.56 h_{ef}$
6	Edge effect (c_{a1}/h_{ef})	0.9 – 1.5		
7	Group effect (s/h_{ef})	0.8 – 3.0		

5 NUMERICAL RESULTS AND DISCUSSION

5.1 Effect of compressive strength f_{cm} on N_u

Three strength values—17.7 Mpa, 32.7 Mpa, and 47.6 Mpa—were used to evaluate the influence of compressive strength on ultimate load. The mechanical properties of the two concrete specimens with strengths of 17.7 MPa and 32.7 MPa were defined according to the equations of CEB-FIP model code 90 (Comité Euro-International du Béton, 1993) (Table 4). The uniaxial behavior curves of concrete under compression and tension and the evolution of damage for these three types of concrete were established according to Section 2.6 and presented in Figure 8.

Table 4. Concrete properties.

ID	Concrete		
	f_{cm}	f_{tm}	E_c
	(Mpa)	(Mpa)	(Gpa)
1	47.6	3.38	39.00
2	32.7	2.56	31.98
3	17.7	1.37	24.59

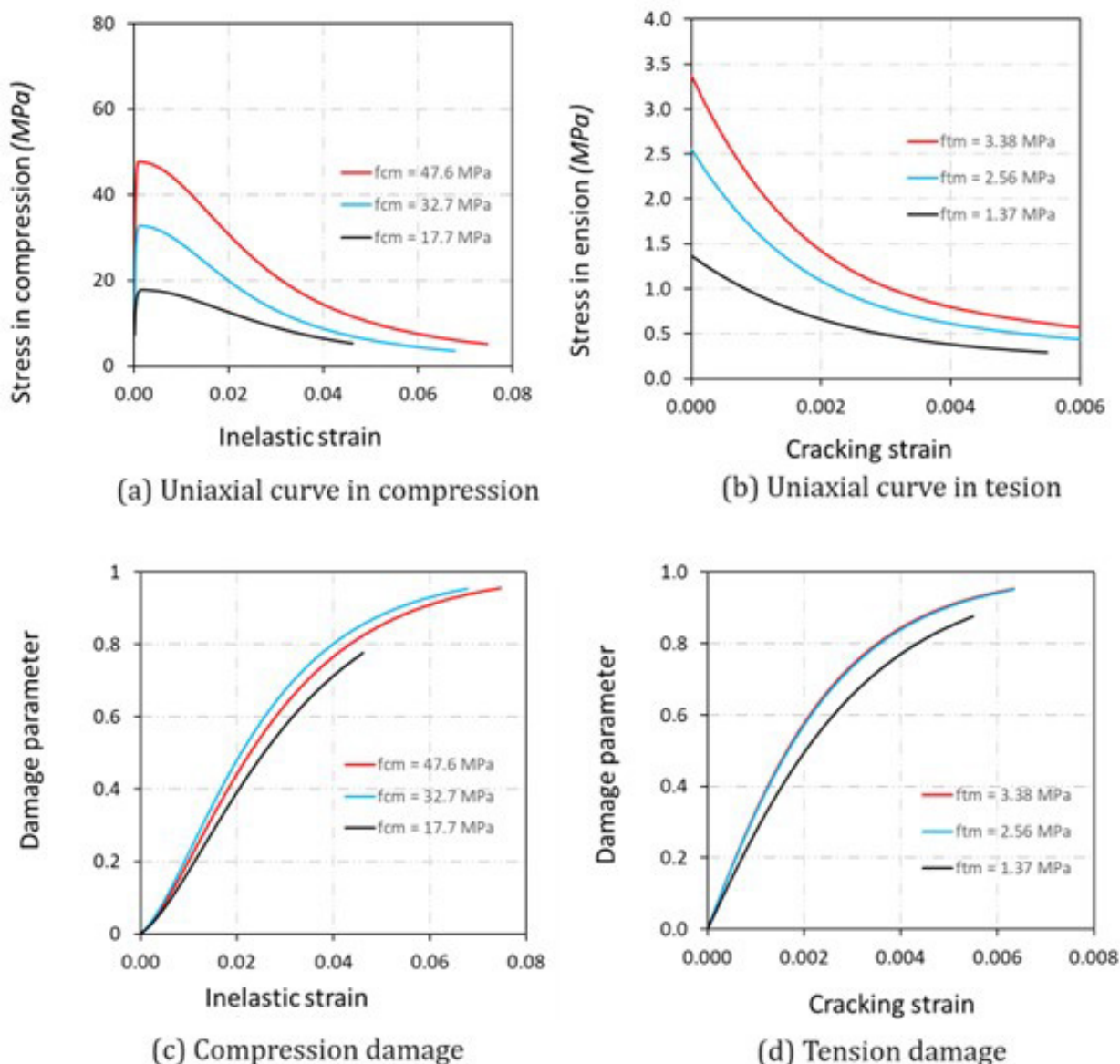


Figure 8. Uniaxial behavior of concrete for parametric study.

Figure 9a and b show the load–slip curves for 60 mm and 120 mm effective embedment depths. It can be observed that only concrete with $f_{cm} = 47.6$ Mpa presented results in favor of safety for both effective embedment depths when compared with the reference values recommended by ACI 318 (2019). Additionally, Figure 9c shows the variation in the ultimate load as a function of the variation in resistance. The ultimate load increased proportionally to the increase in the compressive strength of the concrete: when f_{cm} increased from 17.7 Mpa to 47.6 Mpa with $h_{ef} = 60$ mm, there was an increase of 72%, while with an effective embedment depth of $h_{ef} = 120$ mm, the increase was 95%. This proportionality of the ultimate load at concrete cone failure with the concrete strength is related to the mechanical properties of the concrete: modulus of elasticity E_c and fracture energy G_f .

In contrast, the influence of concrete tensile strength f_{tm} is negligible (Eligehausen et al., 2006) (Eligehausen and Sawade, 1989). Also, according to Eligehausen et al. (2006), the ultimate load at concrete cone failure is proportional to the average compressive strength of the concrete $f_c^{0.5}$. Additionally, increasing the nominal strength of concrete can effectively reduce the compressive deformation of the local concrete under the head and postpone the cracking of the failed concrete, thereby increasing the critical load and critical deformation of the anchor concrete (Zhuang et al. 2021). Similar behaviors were observed in studies by Eligehausen et al. (2006) and Ghimire et al. (2019).

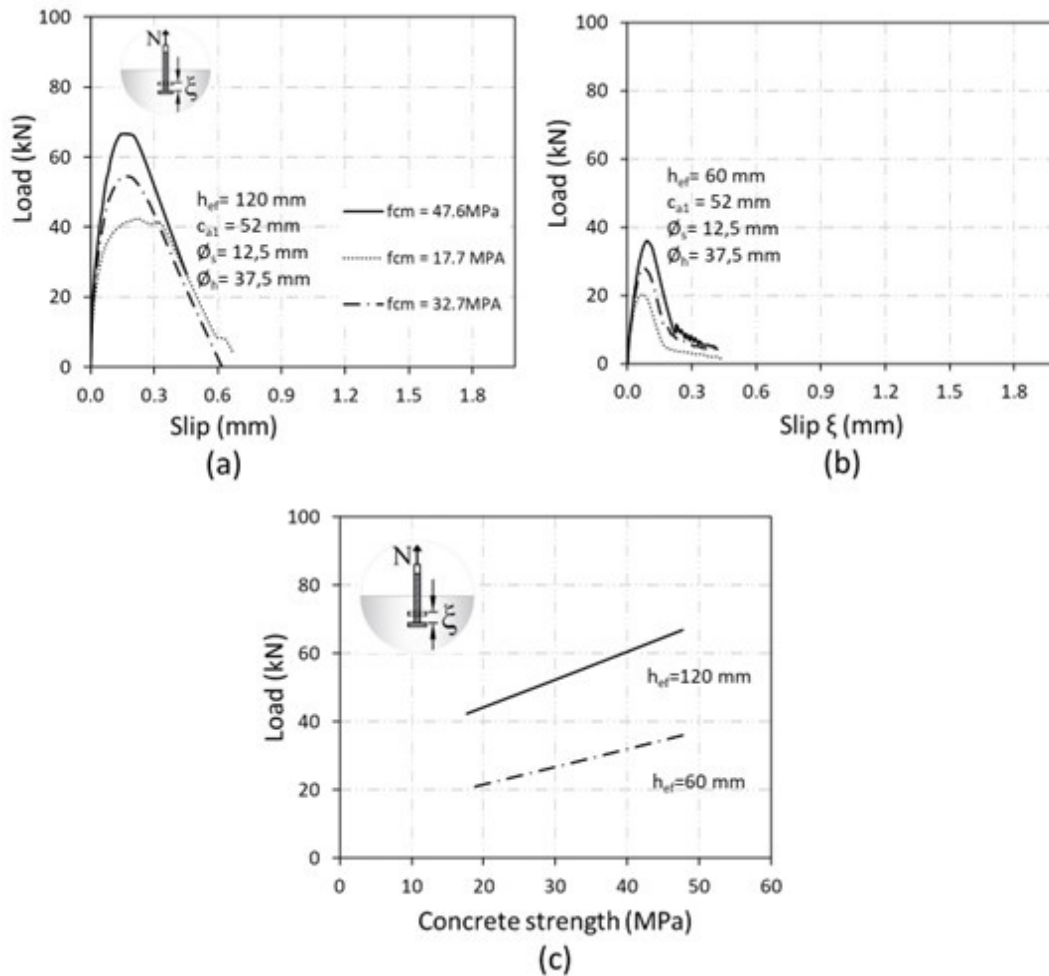


Figure 9. Influence of variation in concrete strength on the ultimate load value N_u : (a) $N_u \times \xi$, $h_{ef} = 120$ mm, (b) $N_u \times \xi$, $h_{ef} = 60$ mm, and (c) N_u vs. f_{cm} .

5.2 Effect of Flexural Reinforcement Ratio on N_u

The effect of the flexural reinforcement ratio was evaluated in the E-60 and G-60 models. For this purpose, flexural reinforcement diameters of 10 mm, 12.5 mm, and 16 mm were used in each model, maintaining the configuration of the initial models and changing only the diameter of the flexural reinforcement. All models had a constant transverse armor of 6.3 mm and the same arrangement. Table 5 presents each model's flexural reinforcement ratios, mechanical properties, and ultimate load results. The mechanical properties of 10 mm and 16 mm steel were determined by Ferreira et al. (2021).

Table 5. Parametric study of the variation in the flexural reinforcement ratio.

Specimen	n°	ϕ_f	Flexural reinforcement			
			f_y (MPa)	E_s (MPa)	ρ_f (%)	N_u (KN)
E-60	4	10	504	190	0.88	35.98
		12.5	557	181	1.38	36.05
		16	545	188	2.26	36.10
G-60	4	10	504	190	1.12	29.72
		12.5	557	181	1.74	30.79
		16	545	188	2.86	31.15

The influence of the flexural reinforcement ratio was studied by Ferreira et al. (2021), who developed experimental tests of headed bars in concrete elements without edge and group effects. Those authors concluded that, for a rate of $0.15\% < \rho_f < 0.60\%$, an average increase of 30% is observed for k_{exp} , which is the modification factor proportional to the tensile strength of the headed bar and which appears to stabilize for $\rho_f > 0.60\%$. Therefore, the flexural reinforcement ratio did not influence the resistance capacity of the concrete cone. A similar result was observed in a study by Nilforoush (2017) on the pullout of headed bars, in which it was concluded that over-reinforced concrete elements have an insignificant effect on anchorage capacity and performance. Therefore, the results of this study are consistent with the results of Nilforoush (2017) and Ferreira et al. (2021).

Still, according to the research by Ferreira et al. (2021), it was observed that increasing the flexural reinforcement ratio increased concrete cracking control and changed the slope of the angle of the concrete cone failure, regardless of the anchorage effective embedment depth. The authors concluded that the specimens with a higher flexural reinforcement ratio presented lower inclinations in the surface angle of the concrete cone failure. The models with a lower flexural reinforcement ratio presented greater surface inclinations. Figure 10 shows the concrete cone failure as a function of the variation in the reinforcement ratio for the E-60 and G-60 models. It is possible to observe that, in group E, the slope of the angle of the concrete cone failure varied between 20° and 23° with an increase in the reinforcement ratio from 0.88% to 2.26%. In group G, the angle varied from 18 to 14, with the reinforcement rate increasing from 1.12% to 2.86%. Based on the ultimate load results presented in Table 5 and the failure mode presented in Figure 10, it is possible to conclude that the reinforcement ratio does not significantly affect the ultimate load but changes the slope of the surface angle of the concrete cone failure. Related results were observed in studies by Ferreira et al. (2021).

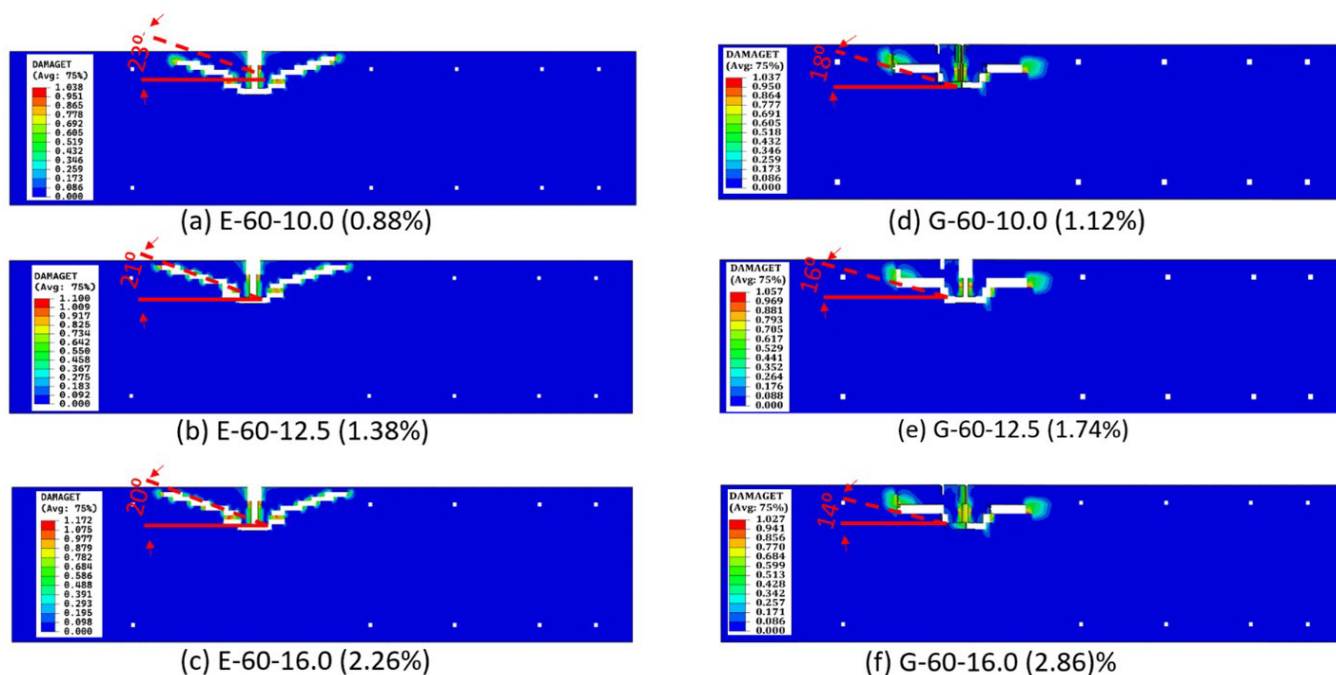


Figure 10: Influence of the flexural reinforcement ratio on the slope of the surface angle of the concrete cone failure.

5.3 Effect of Head Geometry in N_u

The E-60 model was used as an example to investigate the influence of head geometry; the chosen shapes were circular, square, and rectangular. The relationship between the net bearing area of the head and the shaft cross-sectional area was kept the same for all models, equal to $A_{brg}/A_b = 8$, to prevent the size of the head from influencing the ultimate load values. As a result, it was possible to verify that a circular shape is more efficient than the other shapes and that the ultimate load of the concrete cone decreases in the following order: circular > rectangular > square head geometry. The tensile strength of the headed bar was reduced by 21% when the head changed from circular to square. Table 6 presents the ultimate load results depending on the type of geometry head.

Table 6. Ultimate load results as a function of head variation.

ID	Head geometry	h_{ef}	A	B	A_h	A_b	A_{brg}	A_{brg}/A_b	N_u
		(mm)	(mm)	(mm)	(mm ²)	(mm ²)	(mm ²)		(kN)
S1	Square	60	33.23	33.23	1104	122.66	981	8.0	28.50
R1	Rectangular		24.53	45.00	1104	122.66	981	8.0	30.11
C1	Circular		37.50	37.50	1104	122.66	981	8.0	36.05

Note: A_b : shaft cross section (mm²); A_h : gross area of the head (mm); A_{brg} : net bearing area (mm).

5.4 Effect of nominal shaft diameter $d_{s,L}$ on N_u

To evaluate the influence of the nominal diameter of the shaft $d_{s,L}$, reinforcements with diameters of 10.0 mm, 12.5 mm, and 16.0 mm were used, translating to shaft diameter– effective embedment depth relationships $d_{s,L}/h_{ef}$ equal to 0.17, 0.21, and 0.27, respectively. Table 7 shows the ultimate load results as a function of the ratio $d_{s,L}/h_{ef}$. It can be concluded that the ultimate load increases with an increase in the ratio $d_{s,L}/h_{ef}$, varying the shaft diameter from 10 mm to 16 mm for the same effective embedment depths; the ultimate load tended to increase, on average, by approximately 8%.

Shafts with larger diameters produced higher ultimate load values due to the ribs being more prominent in bars with larger diameters, which, in turn, increased the mechanical bond of the shaft with the concrete surface (Sachdeva et al. 2022). This phenomenon was adequately modeled in the numerical simulation because the contact between the concrete and bar shank surfaces was assumed to be a perfect bond. This approach used a surface-based tie constraint model to ensure perfect bonding. This technique joins the two separate surfaces together, constraining each node on the secondary surface to have the same motion as the primary surface so that there is no relative motion between the surfaces (Abaqus 2014). Lima et al. (2020) and Santana et al. (2022) used this same technique to analyze mechanical and nonlinear stresses for adhesion with concrete and steel.

Despite the increase in the ultimate load with the increase in the nominal diameter of the shaft, this 5% increase in the ultimate load is not significant in terms of design. Therefore, the nominal diameter of the shaft has little influence on the resistance capacity of a headed bar under concrete cone failure.

Table 7. Ultimate load as a function of shaft diameter variation.

Specimen	$d_{s,L}$	h_{ef}	$d_{s,L}/h_{ef}$	N_u
	(mm)	(mm)		(kN)
E-60	10	60	0.17	34.99
E-60	12.5		0.21	36.05
E-60	16		0.27	36.89
G-60	10	60	0.17	28.52
G-60	12.5		0.21	30.79
G-60	16		0.27	31.71

Further analysis of the bond mechanism between the shaft and the concrete surface was carried out based on studies by Thompson et al. (2005) and the three example numerical models, E-60-10, E-60-12.5, and E-60-16, as seen in Figure 11. The anchoring of the headed bars was mobilized in two stages. In the first stage, the force was resisted due to the bond near the concrete surface, and the anchoring was conducted entirely based on the bond tension, which peaked at the end of the first stage. This bond is attributed to factors such as chemical adhesion, friction, and mechanical adhesion facilitated by the ribs on the surface of the shaft, according to studies by Chourasia and Gupta (2019).

In the second stage, as the tensile forces in the headed bar exceeded the tensile strength of the concrete, the bond near the surface deteriorated by approximately $0.30N_u$, and the stress in the shaft was more significantly resisted by the head. At the ultimate load N_u , the head tension reached its maximum value, while the bond tension exceeded its peak. As a result of this behavior, concrete cone failure occurred as a combination of peak head stress and reduced peak bond stress. Therefore, these results indicate that the primary mechanism behind the bearing capacity of headed bars is governed by the interlocking of the head with the concrete and less by the connection between the shaft and the concrete. These findings are in line with those found in previous research by Thompson et al. (2005), Ghimire et al. (2019), and Hayek (2023).

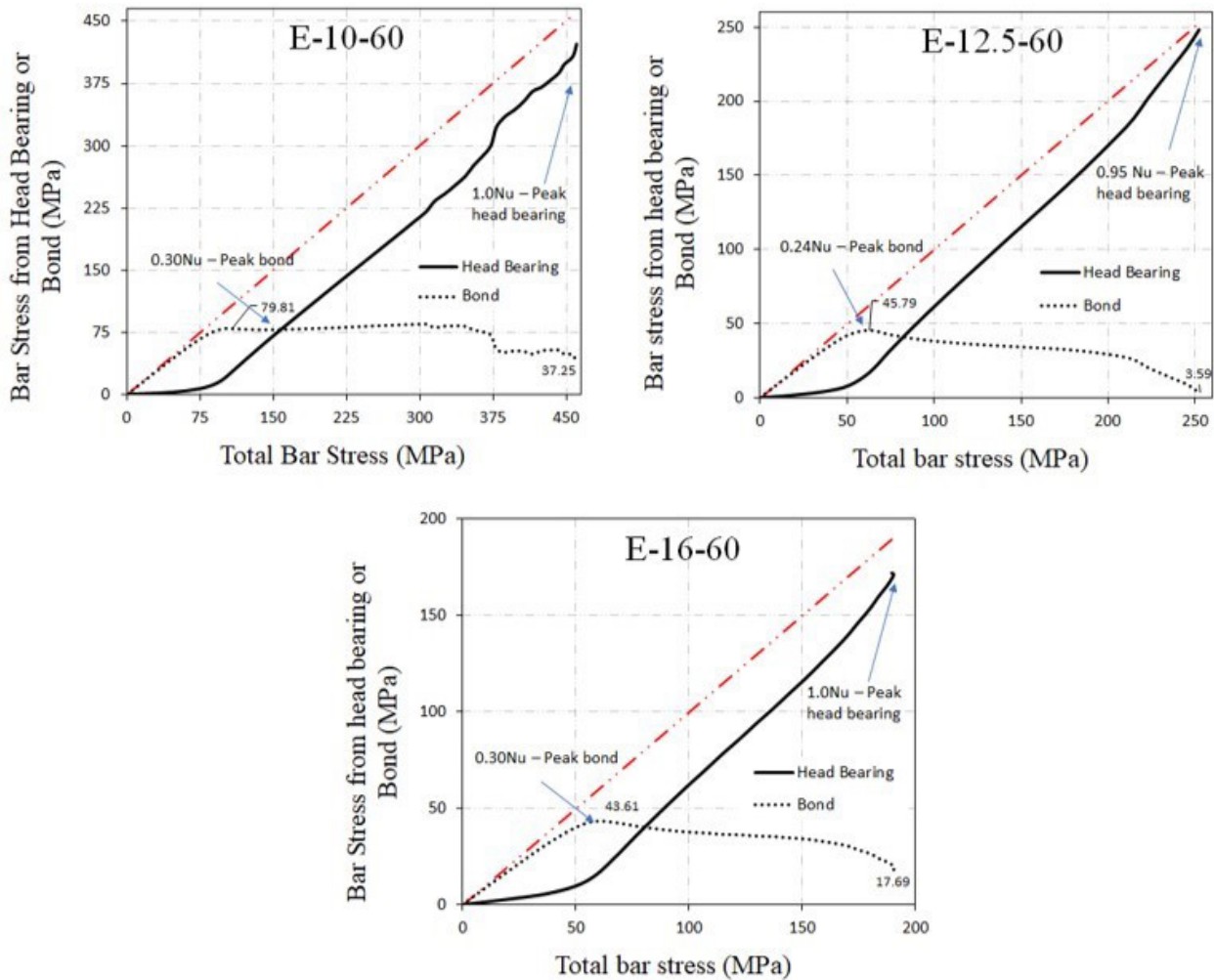


Figure 11: Head tension x shaft tension.

5.5 Effect of head size on N_u

The effect of head size on ultimate load was investigated using two different head sizes: medium $d_h/h_{ef} = 0.31$ and large $d_h/h_{ef} = 0.56$ for the 60 mm and 120 mm embedment depths. The size definition was based on the numerical study of headed bars by Ožbolt et al. (1999), who, in their research, carried out numerical simulations varying the connector head in different sizes for the same embedment depths. The results presented in Table 8 show that the ultimate load of the headed bar increases by 5% on average with the increase in head size. On the other hand, the sliding of the headed bar tended to decrease with the increase in the head regardless of the effective embedment depths. The proximity to the edge did not change the behavior of the slip load curve. These results agree with research by Ožbolt et al. (1999) and Thompson et al. (2005). Figure 12 shows the load-slip results as a function of varying head sizes.

Table 8. Ultimate load and slip values as a function of head diameter d_h

Specimen	d_h (mm)	h_{ef} (mm)	d_h/h_{ef}	ξ (mm)	N_u (KN)
E-60-head (medium)	18.0	60	0.31	0.24	33.14
E-60-head (large)	37.5	60	0.56	0.09	36.05
E-120-head (medium)	37.5	120	0.31	0.16	66.91
E-120-head (large)	62.7	120	0.56	0.12	68.31

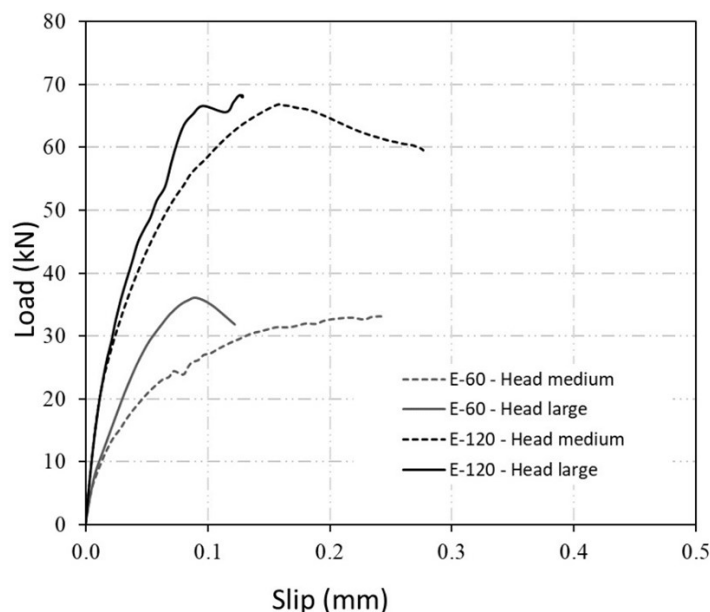


Figure 12. Load-displacement curves calculated for the E-60 E-120 models and two different head sizes: medium and large.

5.6 Edge and group effects on N_u

ACI 318 (2019) establishes that the edge and group effects must be considered for $c_{a1} < 1.5h_{ef}$ and $s < 3h_{ef}$, respectively. To evaluate this influence, seven numerical models were used. The distances from the edge and the spacing between anchors were varied in models with effective embedment depths of 60 mm and 120 mm. Table 9 shows the ultimate load results as a function of the c_{a1}/h_{ef} and s/h_{ef} relationships. The other parameters for developing the models were the same as the validated numerical models. Concrete cone failure prevailed in all simulated models; models 1-3 only evaluated the edge effect with $0.9 < c_{a1}/h_{ef} < 1.5$ and $s/h_{ef} = 3$. The comparison between models 3-6 evaluated only the group effect. Models 4-6 simultaneously assessed the influence of the edge and group effect with $0.9 < c_{a1}/h_{ef} < 1.5$ and $0.80 < s/h_{ef} < 2.0$.

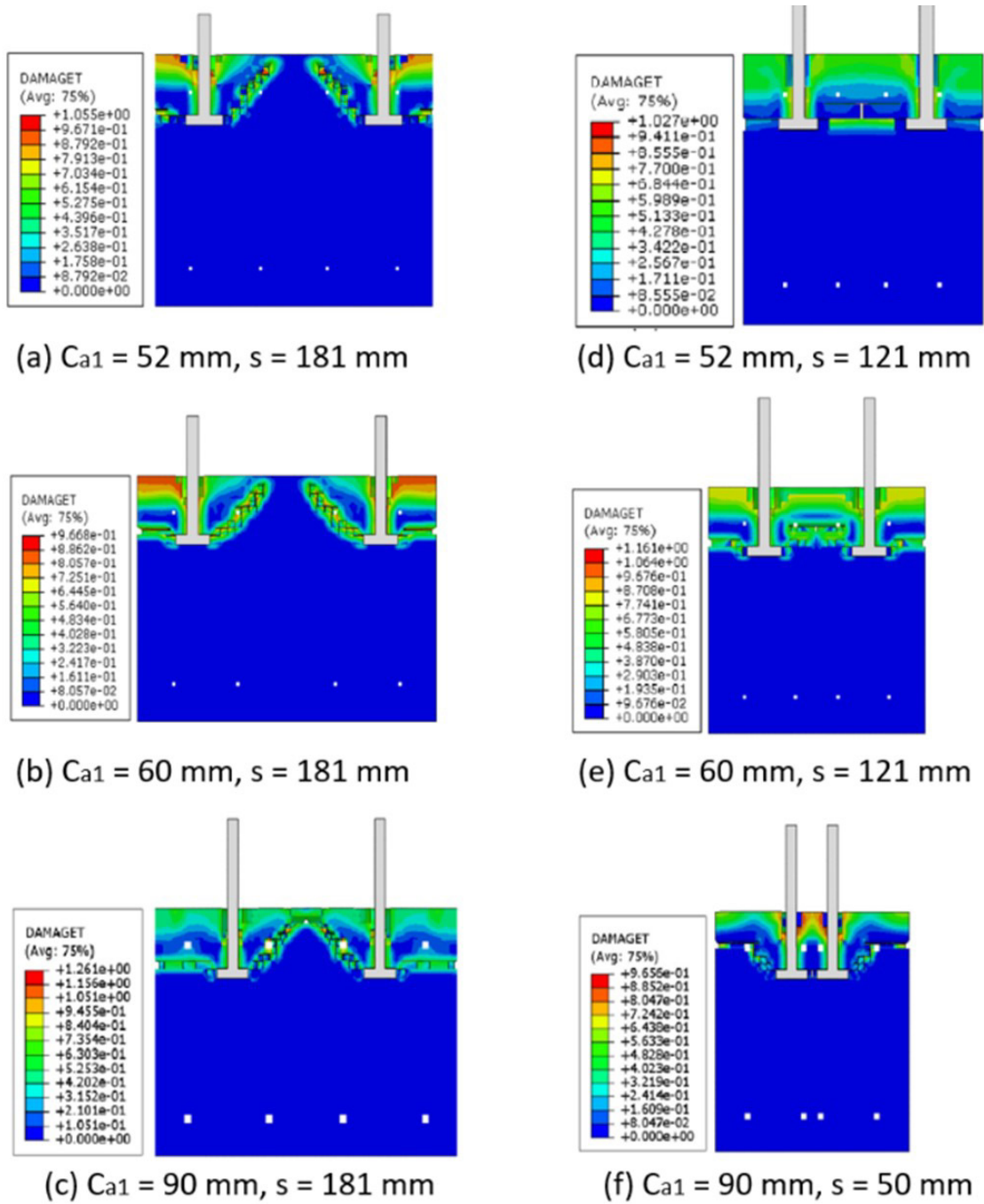
Table 9. Ultimate load results depending on edge and group effects.

ID	Specimen	Type effect	h_{ef} mm	s mm	c_{a1} mm	s/h_{ef}	c_{a1}/h_{ef}	N_u (kN)
1	E-60	edge effect	60	181	52	3.0	0.90	36.05
2	E-60		60	181	60	3.0	1.00	38.46
3	E-60		60	181	90	3.0	1.50	42.92
4	G-60	group effect	60	121	52	2.0	0.90	30.79
5	G-60		60	121	60	2.0	1.00	35.55
6	G-60		60	121	90	2.0	1.50	38.40
7	G-60		60	50	90	0.8	1.50	25.44

The results show that the edge effect tended to reduce the ultimate load of the bar with the head by 6% when the c_{a1}/h_{ef} ratio varied from 1.5 to 1.0 and 10% when the c_{a1}/h_{ef} ratio varied from 1.0 to 0.9 for the same ratio $s/h_{ef} = 3.0$, that is, a maximum reduction of 16% due to the edge effect. It was observed that the simultaneous effect of edge and group tended to reduce the ultimate load by an average of 11% when the s/h_{ef} ratio varied from 3.0 to 2.0, and c_{a1}/h_{ef} varied from 1.5 to 0.9. When the analysis was only related to the group effect, there was a 41% reduction in the ultimate load when the s/h_{ef} ratio varied from 3.0 to 0.8 and $c_{a1}/h_{ef} = 1.5$. Therefore, both the edge and group effects tend to reduce the head bar's ultimate pullout load under concrete cone failure.

Figure 13 shows the crack patterns of specimens from groups E and G. In models with only the edge effect, the proximity to the edge prevented the complete development of the concrete cone failure (Figures 13a, b, and c). Between the headed bars, the failure of the concrete cones resembled the failure of a single-headed bar centered in the concrete, as there was no overlap between them.

In models with the simultaneous edge and group effect, the proximity to the edge also prevented the complete development of the concrete cone. However, due to the tiny space between the anchors, there was a superposition of the concrete cone failures, resulting in a complex double cone failure surface (Figures 13d, e, and f). Studies by Lu and Sonoda (2021) observed similar behavior. Additionally, the ultimate load values of the numerical models of the parametric study with edge and group effects were verified against the calculation model of the ACI 318 (2019) normative prescription. Figure 14 shows the ultimate load values from the numerical model as a function of the ultimate load calculated with ACI 318 (2019). The models presented promising results in favor of safety. However, the G-60 model with $s/h_{ef} = 0.80$ presented an ultimate load value against safety. Therefore, this model is suitable for describing the behavior of bars with heads for values greater than or equal to the ratio $s/h_{ef} = 0.80$.



E – group

G – group

Figure 13. Cracking pattern of models with edge and group effects.

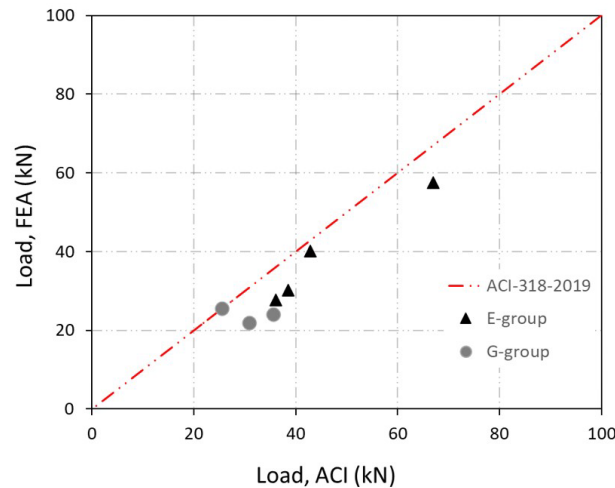


Figure 14. Comparison of the ultimate load FEA of parametric study with ACI 318 (2019).

6 CONCLUSION

In this study, numerical modeling utilizing finite element analysis was implemented via the Abaqus software to investigate the behavior of bars with embedded heads in concrete elements, considering the effects of edges and grouping under direct tensile loads. Adopting a quasi-static solution and the Concrete Plasticity Damage Model achieved accurate replication of the concrete's cracking and crushing and the slippage of the bars with embedded heads. The outcomes derived from the numerical model exhibited remarkable alignment with the benchmark experimental tests, particularly regarding load-slip curves and cracking patterns. This alignment validates the efficacy of the plastic damage model and the quasi-static solution employed in the numerical model.

Furthermore, regarding the validation of the numerical model created against the reference experimental data from the research of Lima (2019) and the validation of the quasi-static solution, the following conclusions can be highlighted:

- The average ratio between the experimental and numerical ultimate loads was 1.02, with a standard deviation of 0.03. The average ratio between the experimental and numerical slippage at the ultimate load was 0.98, with a standard deviation of 0.15.
- The system's energy balance showed that the kinetic energy remained below 5% of the internal energy, indicating that achieving a quasi-static solution with a loading rate of 10 mm/s was possible.
- The numerical models presented the same failure mode as the experimental tests. The angle of the concrete cone failure varied between 16° and 33°; the most significant difference compared to the experimental results was 7°.

With the methodology developed and validated, a parametric numerical study was undertaken, encompassing 19 models wherein various parameters were assessed. These parameters included the concrete compressive strength f_{cm} , the flexural reinforcement ratio ρ_s , the geometry of the head, the diameter of the bar d_s , the $d_{s,L}/h_{ef}$ ratio, the diameter of the head d_h/h_{ef} , and the effects of edge c_{a1}/h_{ef} , and grouping s/h_{ef} . The principal conclusions pertinent to the parametric analysis are summarized in the following section:

- The models in group E with the edge effect confirmed that the ultimate load is proportional to the compressive strength of the concrete $f_{cm}^{0.5}$. The ultimate load increased by 72% when the firm increased from 17.7Mpa to 47.6Mpa for $h_{ef} = 60$ mm. In this same analysis, for $h_{ef} = 120$ mm, the increase was 95%.
- The variation in the flexural reinforcement ratio in the models of groups E and G did not influence the ultimate load results. However, it was observed that the reinforcement ratio changes the slope of the angle of the concrete cone failure. In group E, the angle varied from 23° to 20° when the reinforcement ratio increased from 0.88% to 2.26%, and in group G, the angle varied from 18° to 14° when the reinforcement ratio increased from 1.12% to 2.86%.
- In an analysis of the head geometry, for a ratio $A_{brg}/A_b = 8$, it was concluded that the circular head geometry is more efficient for square and rectangular shapes, with an increase of more than 21% in pullout resistance.

- The size of the nominal shaft diameter has little influence on the resistance capacity of a bar with a head under concrete cone failure. In the same way, the bond between the shaft and the concrete surface has little influence on the tensile strength of the headed bar.
 - The ultimate load increases by an average of 5% when the head size goes from medium to large for embedding lengths of 60 mm and 120 mm, which is insignificant. On the other hand, the slip tended to decrease when the head went from medium to large.
 - The maximum reduction in ultimate load due to the edge effect is 16%, while the group effect reduces it by an average of 41%.
 - The proposed numerical model is suitable for describing the pullout of the bar with a head for a ratio $s/h_{ef} > 0.8$.
- This study showed that the concrete cone strength of headed bars with h_{ef} of 60 mm and 120 mm, embedded in concrete elements under edge and group effects, can be accurately evaluated with a 3D model based on the finite element method. The application of this model allows for predicting the strength of the concrete cone, the failure mode, and the cracking patterns under different installation conditions of headed bars in a structure.

Author's Contributions: Conceptualization, JPB Santos, MH Oliveira, NWB Lima, MJM Pereira Filho and MP Ferreira; Methodology, JPB Santos, MH Oliveira, NWB Lima, MJM Pereira Filho and MP Ferreira; Investigation, JPB Santos, MH Oliveira, NWB Lima, MJM Pereira Filho and MP Ferreira; Writing - original draft, JPB Santos, NWB Lima; Writing - review & editing, MH Oliveira, MJM Pereira Filho, MP Ferreira; Supervision, MH Oliveira.

Editor: Marco L. Bittencourt

References

- Abaqus, V. 6.14 (2014). Documentation. Dassault Systemes Simulia Corporation, v. 651.
- Abed, H. S., Abed, J. M., Al-Rawe, H. S. (2021). Anchorage behavior of headed bars in reinforced concrete beams. In *Structures* 29: 1954-1959.
- ACI Committee 318. (2019). *Building Code Requirements for Structural Concrete*. American Concrete Institute, USA.
- Alfarah, B., López-Almansa, F., Oller, S. (2017). New methodology for calculating damage variables evolution in plastic damage model for rc structures. *Engineering Structures* 132:70-86.
- Alrasyid, H., Yoganata, Y. S., Suluch, M. (2017). Headed reinforcement in concrete structure: State of the art. In *AIP Conference Proceedings* 1903:1.
- ASTM A970M. (2018). *Standard Specification for Headed Steel Bars for Concrete Reinforcement*, ASTM International, West Conshohocken, USA.
- Bokor, B., Sharma, A., Hofmann, J. (2019). Experimental investigations on concrete cone failure of rectangular and non-rectangular anchor groups. *Engineering Structures* 188: 202-217.
- Chourasia, A., Gupta, S. (2019). Influential parameters for headed bars in RC beam-column joint. *Current Science* 116(10): 1666-1673.
- Comité Euro-International du Béton. (1993). *CEB-FIP model code 1990: Design code*. Thomas Telford Publishing.
- DeVries, R. A. (1996). *Anchorage of Headed Reinforcement in Concrete*, Ph.D. Dissertation (in English), The University of Texas at Austin, USA.
- Earij, A., Alfano, G., Cashell, K., Zhou, X. (2017). Nonlinear three-dimensional finite-element modelling of reinforced-concrete beams: Computational challenges and experimental validation. *Engineering Failure Analysis* 82: 92-115.
- Elfgren, L., Cederwall, K., Gylltoft, K., & Broms, C. E. (1982). Fatigue of anchor bolts in reinforced concrete foundations. In *IABSE Colloquium: 17/12/1982: 463-470*. International Association for Bridge and Structural Engineering.
- Eligehausen, R., Mallee, R., Silva, J. F. (2006). *Anchorage in concrete construction (Vol. 10)*, John Wiley & Sons(New York).

- Eligehausen, R., Sawade, G. (1989). A fracture mechanics-based description of the pullout behavior of headed studs embedded in concrete. *Fracture Mechanics of Concrete Structures* 281–299.
- EN 1992-4 (2018). Eurocode 2: Design of concrete structures – Part 4: Design of fastenings for use in concrete, Brussels: European Committee for Standardization.
- Ferreira, M., Pereira Filho, M., Lima, N., Oliveira, M. (2021). Influence of the flexural and shear reinforcement in the concrete cone resistance of headed bars. *Engineering Structures* 248: 1-17.
- Fuchs, W., Eligehausen, R., Breen, J. E. (1995). Concrete capacity design (CCD) approach for fastening to concrete. *ACI Structural Journal* 92(1): 73-94.
- Genikomsou, A. S., Polak, M. A. (2015). Finite element analysis of punching shear of concrete slabs using damaged plasticity model in ABAQUS. *Engineering structures* 98: 38-48.
- Ghimire, K. P., Shao, Y., Darwin, D., O'Reilly, M. (2019). Conventional and high-strength headed bars—Part 2: Data analysis. American Concrete Institute.
- Hayek, Z. N. (2023). Numerical Investigations on the Comparative Study of Headed Studs and Headed Reinforcement, Doctoral thesis (in English), Purdue University, USA.
- Hordijk, D. A. (1992). Tensile and tensile fatigue behaviour of concrete; experiments, modelling and analyses. *Heron*, 37(1): 3-79.
- Karmokar, T., Mohyeddin, A., Lee, J., Paraskeva, T. (2021). Concrete cone failure of single cast-in anchors under tensile loading—a literature review. *Engineering Structures* 243: 112615.
- Ke, Y., Zhang, S. S., Nie, X. F., Yu, T., Yang, Y. M., Jedrzejko, M. J. (2022). Finite element modelling of RC beams strengthened in flexure with NSM FRP and anchored with FRP U-jackets. *Composite Structures* 282: 115104.
- Lai, Z., Han, Y., Yang, X., Wang, Y., Li, Q. (2023). Pullout resistance of stud groups embedded in concrete. *Structures* 47: 1383-1395.
- Lee, J. H., Fenves, G. L. (1998). Plastic-damage model for cyclic loading of concrete structures. *Journal of Engineering Mechanics (ASCE)* 124(8): 892-900.
- Lima, J. M., Bezerra, L. M., Bonilla, J., Silva, R. S., Barbosa, W. C. (2020). Behavior and resistance of truss-type shear connector for composite steel-concrete beams. *Steel and composite structures an international journal* 36(5): 569-586.
- Lima, N. W. B (2019). Tensile strength of pin-type connectors with embedded heads in reinforced concrete elements considering edge effect and group effect. (Master's Dissertation), Publication E.DM - 14A/19, University of Brasília, Brasília, DF, 153p. 2019
- Lu, C., Sonoda, Y. (2021). An analytical study on the pullout strength of anchor bolts embedded in concrete members by sph method. *Applied Sciences* 11(18): 8526.
- Lubliner, J., Oliver, J., Oller, S., Onate, E. (1989). A plastic-damage model for concrete. *International Journal of solids and structures* 25(3): 299-326.
- Marchetto, F. (2015). Use of headed reinforcement bars in construction. PhD Dissertation (in English), Technical University of Madrid, Spain.
- Nilforoush, R. (2017). Numerical and experimental evaluations of load-carrying capacity of cast-in-place headed anchors and post-installed adhesive anchors, Doctoral dissertation (in English), University of Lulea, Sweden.
- Ožbolt, J., Eligehausen, R., & Reinhardt, H. W. (1999). Size effect on the concrete cone pullout load. *Fracture Scaling*, 95: 391-404.
- Qureshi, J., Lam D., Ye, J. (2011). Effect of shear connector spacing and layout on the shear connector capacity in composite beams, *Journal of Constructional Steel Research* 67: 706-719.
- Ribeiro, P. D. O., Gidrão, G. D. M. S., Vareda, L. V., Carrazedo, R., Malite, M. (2020). Numerical and experimental study of concrete I-beam subjected to bending test with cyclic load. *Latin American Journal of Solids and Structures* 17.
- Sachdeva, P., Roy, A.B. D., Kwatra, N. (2022). Behavior of headed bars in steel fibers-based concrete, *Sādhanā* 48:4.
- Santana, P. F., Silva, P. C., Ferreira, M. P., Bezerra, L. M., Oliveira, M. H. (2022). Experimental and numerical study of headed bars embedded in RC members under tension. *Structural Engineering and Mechanics* 84(4): 531-546.

- Shafei, E., Tariverdilo, S. (2021). Seismic pullout behavior of cast-in-place anchor bolts embedded in plain concrete: Damage plasticity based analysis. *Structures* 34: 479-486.
- Thompson, M. K., Ziehl, M. J., Jirsa, J. O., Breen, J. E. (2005). CCT nodes anchored by headed bars-Part 1: Behavior of nodes. *ACI Structural Journal* 102(6): 808.
- Zhuang, L. D., Chen, H. B., Ma, Y., Ding, R. (2021). Research on whole-process tensile behavior of headed studs in steel–concrete composite structures. *International Journal of Concrete Structures and Materials*, 15(1): 24.